PHYSICAL REVIEW MATERIALS **8**, 046201 (2024)

Charge state and entropic effects affecting the formation and dynamics of divacancies in 3C-SiC

Cunzhi Zhang,[1] Francois Gygi,[2] and Giulia Galli[1,3,4,*]
[1]*Pritzker School of Molecular Engineering, University of Chicago, Chicago, Illinois 60637, USA*
[2]*Department of Computer Science, University of California Davis, Davis, California 95616, USA*
[3]*Department of Chemistry, University of Chicago, Chicago, Illinois 60637, USA*
[4]*Materials Science Division and Center for Molecular Engineering, Argonne National Laboratory, Lemont, Illinois 60439, USA*

(Received 8 January 2024; accepted 22 March 2024; published 5 April 2024)

Using nudged elastic band calculations and first-principles molecular dynamics with enhanced sampling, we study the formation and dynamics of the divacancy V_CV_{Si} (VV) in cubic silicon carbide, including VV rotation and migration. We show that for all processes studied here the energy barriers and preferred pathway depend on the charge state of the defects. Our results indicate that the influence of multiple charge states and entropic effects should be considered for a quantitative description of the physical and dynamical properties of point defects at finite temperatures. In addition, we demonstrate that molecular dynamics simulations using machine-learning potentials can efficiently and reliably capture entropic effects and yield accurate free-energy barriers.

DOI: 10.1103/PhysRevMaterials.8.046201

I. INTRODUCTION

Silicon carbide (SiC) is a wide band gap semiconductor with outstanding properties [1,2], desirable for high power and high-temperature electronics [1,3], as well as nuclear applications [4,5]. Furthermore, mature growth, doping, and nanofabrication techniques are available for SiC, enabling its manufacturability on a wafer scale [1,6,7]. In recent years, SiC has also attracted great interest as a host crystal for optically active spin defects (point defects known as color centers) [6–9], which are appealing candidates for, e.g., quantum sensing and quantum communication applications. The most studied color centers in SiC include the silicon vacancy (V_{Si}), the divacancy V_CV_{Si} (VV), and the nitrogen-vacancy pair N_CV_{Si}. In particular, the VV exhibits attractive properties, such as optical addressability [10], long coherence times [11], spin-to-charge conversion [12], as well as a near-infrared spin-photon interface [13].

Important to the scalable implementation and device integration for quantum technologies is a fine control over the formation of spin defects, in terms of their spatial location, population, and charge states [6,7,14–17]. In SiC, spin defects are commonly created via electron irradiation, ion implantation or pulsed laser, followed by a high-temperature (T) annealing process [6,7,14,15]. The annealing treatment is essential, as dopants, interstitials, or vacancies become mobile and reactions between them can occur; the annealing process leads not only to the healing of the lattice damage but it can also be engineered to drive the formation of specific, desired defects. Therefore, a detailed knowledge of defects' stability, kinetics, and defect-defect reactions at high-T is critical to design and optimize experimental parameters to generate qubit centers in a controlled manner.

In this context, theoretical modeling based on density functional theory (DFT) is a useful tool, due to its predictive power and the fact that it can provide a quantitative understanding of defect stability and formation. For example, several studies for the VV were reported investigating, e.g., its formation energy (stable charge state) [18–20], reorientation mechanism [21,22], the pairing of V_{Si} and the carbon vacancy (V_C) to form VV [20,21], as well as the aggregation of VV with additional V_{Si} or V_C to form larger vacancy clusters [20,23]. Recently, we proposed a general computational protocol based on DFT to investigate the formation of point defects at the atomistic level [24], which was then applied to the study of VV in 3C-SiC, providing insights into the VV formation mechanism as a function of T and Fermi level (E_F). Specifically, we computed the energy barrier (E_b) for various pathways as a function of the charge state (q) of the defect, where the effect of the spin degree of freedom was implicitly included, and we estimated entropy changes (ΔS) from the initial to the transition state at a given temperature for several paths in 3C-SiC. Assuming the validity of the harmonic approximation and of classical statistics, the free-energy barriers (G_b) as a function of T at a fixed lattice constant were obtained as

$$G_b(T, q) = E_b(q) - T\Delta S, \tag{1}$$

which were then used to compute the activation temperature (T_a) for several defect processes. In Ref. [24], we used the same ΔS for all pathways and charge states. Specifically, we accounted for the entropic effects on G_b [the $-T\Delta S$ term in Eq. (1)] due to the thermal excitation of phonons at finite T, with T-independent phonon frequencies, at a fixed lattice constant.

In this paper, we provide additional results on the formation and dynamical properties of the VV in 3C-SiC, by considering in detail the effect of charge states and path-dependent entropy. We consider various atomic pathways and

---

[*] gagalli@uchicago.edu

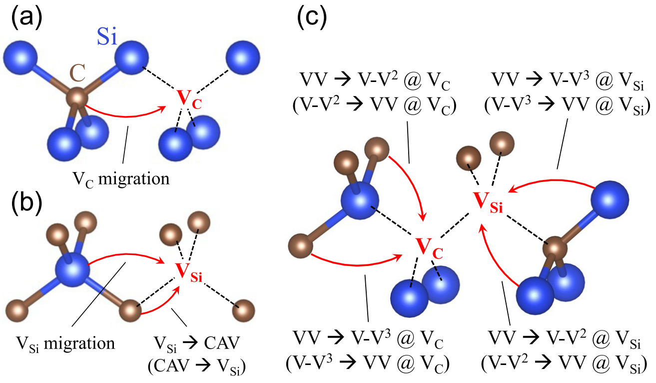

FIG. 1. Atomic pathways relevant to the divacancy (VV) formation. (a) Carbon vacancy (V_C) migration. (b) Silicon vacancy (V_{Si}) migration; V_{Si} and carbon-antisite-V_C complex (CAV) interconversion. (c) VV and the neighboring V_C-V_{Si} pair (V-V) interconversion. V-V^2 (V-V^3) denotes the V-V pair where V_{Si} resides at the second (third)-neighboring site of V_C. VV can convert into V-V^2 (V-V^3) via: (1) the migration of V_C within VV away from the adjacent V_{Si} denoted as VV → V-V^2 @ V_C (VV → V-V^3 @ V_C); and (2) the migration of V_{Si} within VV away from the adjacent V_C denoted as VV → V-V^2 @ V_{Si} (VV → V-V^3 @ V_{Si}). We indicate the atomic pathway associated to each red arrow and the red arrow specifies the atomic motion; we indicate the reverse (or backward) process in parenthesis if the initial and final states of the path are different. In our notation, the defect on the left (right)-hand side of the arrow corresponds to the initial (final) state of a path. For example, for the V-V^3 → VV @ V_C path, the initial (final) state is the V-V^3 (VV) defect.

analyze the dependence of the barrier E_b on the charge state q, and the entropic effects due to the thermal excitation of phonons in determining the value of G_b at finite temperatures, at a fixed lattice constant. Further, we discuss the activation temperature T_a and atomic mechanisms for the VV rotation and migration processes, which were not considered in Ref. [24].

The rest of the paper is organized as follows. In Sec. II, we describe the methodologies used in our paper and computational details. In Sec. III, we present our results with conclusions given in Sec. IV.

II. METHODS

We considered multiple point defects and their transformation pathways in 3C-SiC. Specifically, we investigated the V_C, V_{Si}, VV, the carbon-antisite (C_{Si})-V_C complex (CAV), the neighboring V_C-V_{Si} pairs (V-V), where V_{Si} is located at the second (third)-nearest site of V_C, denoted as the V-V^2 (V-V^3) and the $V_C C_{Si} V_C$ complex (VCV); their geometries can be found in Figs. 1 and 2. DFT calculations and the nudged elastic band method were employed to compute the energy barriers for several dynamical processes involving the formation and transformation of point defects. The free-energy surfaces (FES) and the free-energy barriers were determined with enhanced sampling calculations using both classical and first-principles molecular dynamics (MD) simulations. We analyzed the change of free-energy barriers at finite temperature due to entropic effects using the harmonic approximation and classical statistics, since we are mainly concerned with high-T properties, and we obtained free-energy barriers using MD simulations, which treat atoms as classical particles. In all calculations, we used 216-atom cubic supercells with the lattice constant of 13.248 Å, constructed from the 3C-SiC cell with lattice constant of 4.416 Å. This lattice constant was determined by carrying out a first-principles MD (FPMD) simulation using the Perdew-Burke-Ernzerhof (PBE) functional [25] in the NPT ensemble (at 1500 K and zero pressure). We used the lattice constant of 4.416 Å to approximately include the lattice expansion effects induced by the high annealing temperatures (> ~1000 K to generate VV), as compared to the measured value of 4.36 Å at 0 K [26]. Nonetheless, we found that the relaxed defect geometries using the lattice constant of 4.416 Å and 4.36 Å are only slightly different, so do the computed energy barriers (see Supplementary Information in Ref. [24]). Based on a polynomial fitted to the measured data [27], we obtained a lattice constant of 3C-SiC at 1500 K of 4.382 Å. Hence, the lattice constant used in this paper is a slight overestimate (~0.8%) of the experiment, which we consider to be a minor difference.

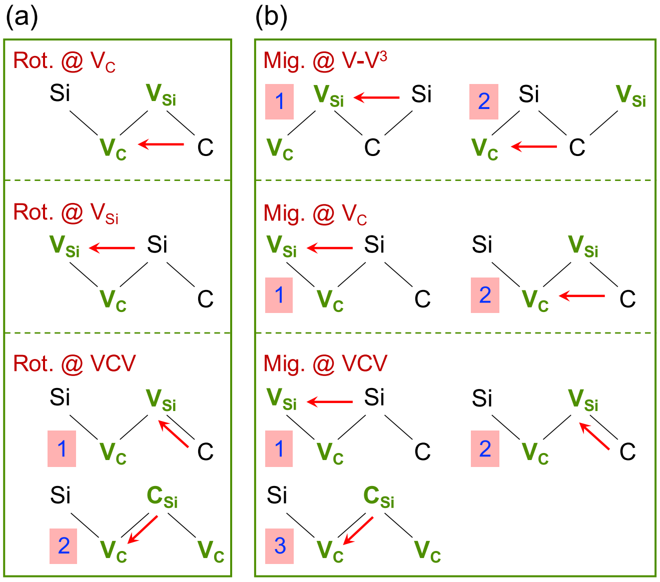

FIG. 2. Atomic pathways for the divacancy (VV) rotation and migration. (a) Three VV rotation paths. VCV refers to the $V_C C_{Si} V_C$ complex. (b) Three VV migration paths. For multiple-step processes, we use numbers to indicate the order of the process. We note that for each of these paths the initial and final states are the same.

Below we present specific details for each of our calculations.

A. Energy barrier and activation temperature calculations

We first summarize the computational methods, which were also used in Ref. [24].

The energy barriers (E_b) for a given defect process were computed by using the climbing-image nudged elastic band (NEB) method [28], and by coupling the QBOX [29] and the PASTA [30] codes, adopted for DFT and NEB calculations respectively. In DFT calculations, we used the PBE functional, optimized norm-conserving Vanderbilt (ONCV)

TABLE I. Energy barriers E_b (eV) obtained from NEB calculations at the DDH level of theory. We show results for the pathways shown in Figs. 1 and 2 at charge state q from 2 to –2. For those paths for which the initial and final states are different (see Fig. 1), we show E_b for both the forward and backward processes (see Methods); values in parenthesis are for the backward processes.

	E_b				
Pathways	$q = +2$	$q = +1$	$q = 0$	$q = -1$	$q = -2$
$\mathrm{V_C}$ migration[a]	5.22	4.36	3.87		
$\mathrm{V_{Si}}$ migration	3.78	3.72	4.05	3.56	2.77
$\mathrm{V_{Si}} \rightarrow$ CAV	2.04 (5.79)	2.11 (4.25)	3.63 (3.52)	3.83 (2.55)	3.74 (2.16)
$\mathrm{V\text{-}V^2} \rightarrow \mathrm{VV}$ @ $\mathrm{V_C}$	2.15 (3.66)	2.54 (5.15)	2.56 (5.2)	2.67 (5.31)	2.59 (5.46)
$\mathrm{V\text{-}V^2} \rightarrow \mathrm{VV}$ @ $\mathrm{V_{Si}}$	2.4 (3.9)	2.38 (4.97)	1.89 (4.53)	1.45 (4.08)	0.89 (3.76)
$\mathrm{V\text{-}V^3} \rightarrow \mathrm{VV}$ @ $\mathrm{V_C}$	2.84 (4.11)	2.78 (4.64)	2.47 (4.61)	2.46 (4.71)	2.46 (4.82)
$\mathrm{V\text{-}V^3} \rightarrow \mathrm{VV}$ @ $\mathrm{V_{Si}}$	2.17 (3.44)	1.9 (3.76)	0.9 (3.04)	0.7 (2.95)	0.53 (2.89)
Rot. @ $\mathrm{V_C}$[b]		5.14	5.69	5.21	5.18
Rot. @ $\mathrm{V_{Si}}$	3.79	3.84	3.23	3.05	2.47
Rot. @ VCV	1.88	3.3	3.79	3.96	4.43
Mig. @ $\mathrm{V\text{-}V^2}$	3.9	4.97	5.2	5.31	5.45
Mig. @ $\mathrm{V\text{-}V^3}$	4.11	4.64	4.61	4.71	4.82
Mig. @ $\mathrm{V_C}$[b]		5.14	5.69	5.21	5.18
Mig. @ VCV	3.79	3.84	3.79	3.96	4.43

[a] For carbon vacancy ($\mathrm{V_C}$), we considered q from 2 to 0.

[b] At charge state $q = 2$, the pathway is not stable and transforms into a different pathway.

pseudopotentials [31], a 2 × 2 × 2 Monkhorst-Pack (MP) grid and a 60 Ry cutoff for the plane-wave basis set. In NEB calculations, we used a spring constant of 2 eV/Å^2 and a force tolerance of 0.02 eV/Å to obtain converged results. We explored the charge state q of defects from +2 to –2, except for $\mathrm{V_C}$ where q varied from +2 to 0, and considered different spin states. Specifically, we determined the most stable spin state of a given defect for each NEB image at a given q, and then used the corresponding total energy and atomic forces to update the NEB images. However, we found that considering different spin states only slightly influences the computed E_b. The obtained E_b were denoted as $E_\mathrm{b}^\mathrm{PBE}$@222, and summarized in Table SI within the Supplemental Material [32]. When the initial and final states of a path turned out to be different, we report the E_b for both the forward (from the initial to the transition state) and the backward (from the final to the transition state) processes.

After determining the $E_\mathrm{b}^\mathrm{PBE}$@222 as a function of q at the PBE level of theory, single-point energy calculations with both the PBE and the dielectric-dependent hybrid functionals [33] (DDH; 15% exact exchange) were performed. For those calculations, we used the ONCV pseudopotentials, the Γ point and a 60 Ry cutoff for the plane-wave basis set. Based on the converged minimum energy path obtained in NEB calculations, the total energy of each image was evaluated using both the PBE and the DDH functional from a single-point calculation; we then calculated the energy barrier as the total energy difference between the initial (or final) and the transition state of a path; the energy barrier obtained from the total energies at the PBE (DDH) level of theory is denoted as $E_\mathrm{b}^\mathrm{PBE}@\Gamma$ ($E_\mathrm{b}^\mathrm{DDH}@\Gamma$). To improve the overall accuracy of the results computed at the PBE level of theory, we computed the barrier correction as $\Delta E_\mathrm{b} = E_\mathrm{b}^\mathrm{DDH}@\Gamma - E_\mathrm{b}^\mathrm{PBE}@\Gamma$; the correction was then applied to the PBE results. Specifically, we estimated the energy barriers at the DDH level of theory as $E_\mathrm{b}^\mathrm{PBE}@222 + \Delta E_\mathrm{b}$, denoted as $E_\mathrm{b}^\mathrm{DDH}$@222. We found that ΔE_b calculated with the Γ point and the 2 × 2 × 2 MP grid are close to each other. The $E_\mathrm{b}^\mathrm{DDH}$@222 values were used to obtain our final results, and they are summarized in Table I. In general, the energy barriers computed with the DDH functional turned out to be higher than those obtained with the PBE functional, which can be seen by comparing the results in Table I and Table SI within the Supplemental Material [32]. This result is consistent with several findings in the semiconductor literature indicating that local or semilocal functionals underestimate energy barriers [34–37] in semiconductors.

We found that the transition between different charge states is a fast process, compared to the transition of defects into different configurations at high temperature (see Supplementary Information in Ref. [24]). A given process can occur via multiple, competing channels, each with a different charge state of the defect, and therefore we computed an effective barrier ($E_\mathrm{b,EFF}$),

$$E_\mathrm{b,\,EFF}(E_\mathrm{F}) = \min_{q}\{\Delta E_\mathrm{f}(q, E_\mathrm{F}) + E_\mathrm{b}(q)\}, \tag{2}$$

where $\Delta E_\mathrm{f}(q, E_\mathrm{F}) = E_\mathrm{f}(q, E_\mathrm{F}) - \min_{q}\{E_\mathrm{f}(q, E_\mathrm{F})\}$ is the formation energy difference relative to the most stable charge state, for a given value of the Fermi level (E_F), as evaluated in Ref. [24]; E_f is the formation energy of a defect (initial state of the path); E_b is the barrier from the initial to the transition state of the path at the DDH level of theory. In our calculations, we also considered thermodynamically unstable charge states, which, importantly, may lead to pathways of lower $E_\mathrm{b,EFF}$ than those involving only thermodynamically stable states. Further, the defect charge state was assumed not to change during the defect geometrical transformations, due to the short lifetime of the barrier crossing event. Spin-state transitions are allowed at high temperatures and implicitly included in our calculations of E_b. However, further investigations of spin-state transitions, e.g., by estimating their timescale at high T, will be important.

We emphasize that the differences between our calculated values of E_b when we consider or neglect the spin-state transition along the path are minor (see also Methods in Ref. [24]).

Finally, based on our results for $E_\mathrm{b,EFF}$, we computed the activation temperature (T_a) for the defect processes of interest. The T_a, defined as the temperature above which a process is thermally activated, is proportional to $E_\mathrm{b,EFF}$ [24], i.e., $T_\mathrm{a} = C \times E_\mathrm{b,EFF}$. The prefactor C depends on several quantities, including the entropy change from the initial to the transition state of a path. In Ref. [24], we estimated $C \approx 331$ K/eV for SiC, and this value is used throughout this paper. We note that, similar to $E_\mathrm{b,EFF}$, T_a is a function of E_F.

B. Free-energy surface and free-energy barrier calculations

We performed both classical and first-principles simulations to model the defect dynamics. In our first-principles simulations, we used the DFT method with the PBE functional and the QBOX code, with ONCV pseudopotentials, the Γ point and a 40-Ry cutoff for the plane-wave basis set. In our classical simulations, carried out with the LAMMPS code [38,39], we used interatomic potentials that are described next, and include empirical force fields (FF) and a machine-learning potential derived from a DFT training set.

1. *Interatomic potentials*

The empirical FFs used here are: the Gao-Weber potential (GW) [40], the environment-dependent interatomic potential (EDIP) [41], the modified embedded-atom method potential (MEAM) [42], and the Tersoff potential (TERSOFF) [43].

To derive the machine-learning FF, we used the moment tensor potential (MTP; model level of 20) [44,45], with a cutoff distance of 5 Å. We selected snapshots from FPMD trajectories every ~1 ps (see Sec. II B 3), for a total of 1302 configurations. Their corresponding atomic positions, total energies, and atomic forces were used as the initial training data, to obtain the initial-MTP, which was then used, with the Maxvol algorithm [46], to select a set of representative configurations from FPMD trajectories (see Sec. II B 3) [44], for a total of 371 configurations. Their corresponding atomic positions, total energies, and atomic forces constituted the final dataset, on which we trained a MTP potential for production runs.

The training error (root-mean-square error) of the energy obtained with the MTP potential is 1.2 meV/atom and that on the forces is 0.11 eV/Å. We verified that increasing the cutoff distance to 6.5 Å slightly changes the training error, to 1.4 meV/atom for the energy (no change was observed for the forces). We emphasize that our FPMD trajectories were obtained from enhanced sampling calculations with the adaptive biasing force (ABF) method [47] and thus the configurational space of defect transformation processes was efficiently sampled.

Only three defect processes in the neutral-charge state were included in the training set for the MTP (V-V^3 $\rightarrow$ VV @ V$_\mathrm{C}$, V-V^3 $\rightarrow$ VV @ V$_\mathrm{Si}$ and Rot. @ V$_\mathrm{Si}$; these processes are discussed in detail in Secs. II B 3 and III A). Our aim is not to obtain a MTP potential that can be used for multiple defect pathways at various temperatures, as a function of charge state, but rather to understand the performance of the MTP in modeling specific defect processes in semiconductors. Hence we focused on the MTP performance on few pathways to gain some general insights.

2. *Constrained optimizations*

We performed constrained optimizations to compute the potential-energy surfaces (PES) at $T = 0$ K, where the lattice parameters of the supercell were kept fixed, the degree of freedom (DOF) of interest, i.e., the collective variable (one-dimensional; see Sec. II B 3) was kept fixed and the remaining DOFs of the system were relaxed during the minimization process. Specifically, the constrained optimization was implemented as

$$\mathbf{x}^0 = \underset{\mathbf{x}}{\mathrm{argmin}}\,\{U(\mathbf{x}) + K \times (\xi(\mathbf{x}) - \xi^0)^2\}, \tag{3}$$

$$U(\xi^0, T = 0\ \mathrm{K}) \approx U(\mathbf{x}^0), \tag{4}$$

where U is the potential energy; ξ is the collective variable (see Sec. II B 3); ξ^0 is the collective variable value at which we evaluate the potential energy of the system; $\mathbf{x}$ are the atomic coordinates; K is a tunable parameter. The function U as a function of ξ ($U(\xi, T = 0\ \mathrm{K})$) is the PES at $T = 0$ K, evaluated either with one of the interatomic potentials (described in Sec. II B 1) or with DFT calculations (described in Sec. II B). In actual calculations, K needs to be sufficiently large, so that after structural relaxations the collective variable of the system ($\xi(\mathbf{x}^0)$) is close to ξ^0.

We considered ξ^0 on a evenly spaced grid (one dimensional), and we performed constrained optimizations sequentially at each ξ^0 along the grid, by initializing the calculation at the i grid point based on the value of $\mathbf{x}^0$ obtained from the calculation at the $i-1$ or $i+1$ grid point. By doing so, the energy change along the collective variable could be continuously monitored. We considered both the forward and the backward processes of any given path, by first constraining the system from the initial to the final state of the path and thus obtaining the PES at $T = 0$ K for the forward process, and a final-state configuration. Based on the latter, we then constrained the system from the final to the initial state of the path, and obtained the PES at $T = 0$ K for the backward process. The difference in results between the forward and backward processes is indicative of either hysteresis or the presence of metastable configurations.

The PESs determined above were then used to evaluate the energy barriers at $T = 0$ K for both the forward and backward processes, which are equivalent to the energy barriers calculated via the NEB method (see Sec. II A).

The same lattice constant was used to compute the PES at 0 K and the FES at 1500 K (see Sec. II B 3); the difference between the two does not contain contributions from the lattice expansion, and can be used to understand the entropic effects due to the thermal excitation of phonons at a fixed lattice constant (see discussion in Sec. II B 4).

We computed the PESs at $T = 0$ K for four pathways (see Sec. II B 3). In first-principles simulations, only the neutral-charge state was considered; we studied the V$_\mathrm{C}$ migration in the singlet-spin state, while for all other paths we considered the triplet-spin state, to be consistent with the cases treated in our classical simulations with empirical FFs, where no charge is associated to sites or atoms, and with the MTP potential, which was trained for the neutral-charge state.

3. Enhanced sampling calculations

We performed enhanced sampling calculations to compute the free-energy surfaces at a finite temperature, i.e., $T = 1500$ K, by coupling the SSAGES code [48] with the QBOX and the LAMMPS codes, where SSAGES is the engine driving the enhanced sampling calculations. We used the ABF method [47], and we utilized the one-dimensional collective variable (CV) ξ [49] defined as

$$\xi = (\mathbf{R} - \mathbf{R}_{\text{gate}}) \cdot \mathbf{e}_{\text{projection}}, \tag{5}$$

where $\mathbf{R}$ are coordinates of the moving atom, either C or Si atom; $\mathbf{R}_{\text{gate}}$ is the center of mass for a group of atoms, named gate atoms; $\mathbf{e}_{\text{projection}}$ is the unit projection vector.

In classical simulations, we considered four atomic pathways (see Sec. III A): (1) V_C migration; (2) V-V^3 → VV @ V_C; (3) V-V^3 → VV @ V_{Si}; and (4) Rot. @ V_{Si}, with the CVs used for these paths given in Fig. S1 within the Supplemental Material [32]. For each of them, we carried out one single MD simulation of 1.5 ns at 1500 K in the NVT ensemble, with a time step of 1 fs and the MTP potential.

However, in FPMD simulations, we restricted our attention to three pathways: V-V^3 → VV @ V_C, V-V^3 → VV @ V_{Si}, and Rot. @ V_{Si}, for which only the neutral-charge state and the triplet-spin state were considered. For each path, we carried out FPMD simulations at 1500 K in the NVT ensemble, with a time step of 1 fs; we launched 62 independent FPMD simulations ($\sim$6 ps each) and in total we obtained a $\sim$370 ps trajectory, employing the PBE functional to compute the electronic structure and atomic forces (see Sec. II B).

Based on the FESs obtained above, we computed the free-energy barriers. Using the results from classical MD simulations, we examined the convergence of free-energy barriers with respect to the simulation time and found that they were well converged already for $\sim$400 ps simulations. The free-energy barriers obtained from 360 ps and 1.5 ns simulations differ by $<\sim 0.02$ eV, indicating that in FPMD simulations of $\sim$370 ps our results were converged.

4. Harmonic approximation

We employed the harmonic approximation to compute the free energy, as a function of T, for several defects, and evaluated the free energy of the initial, final, and transition states of a given path; the free-energy difference between the initial (final) and the transition state corresponds to the free-energy barrier (G_b) for the forward (backward) process. We computed the free energy according to classical mechanics, since all atoms are classical particles in our MD simulations and verified that the values of G_b obtained using classical and quantum statistics are close at $T = 1500$ K, their difference being $< \sim 0.01$ eV.

Assuming a system with N atoms, the free energy G is given by [50–52]

$$G(T) = U + \sum_{i}^{3N-3} k_B T \ln\left(\frac{\hbar\omega_i}{k_B T}\right), \tag{6}$$

where U is the potential energy at $T = 0$ K; k_B is the Boltzmann constant; ω_i is the frequency of the ith phonon mode. We excluded three modes of zero frequency.

To be consistent with our enhanced sampling calculations, the phonon mode corresponding to the CV DOF [50,51] was excluded from the summation. For the transition state, it amounted to simply excluding the phonon mode with negative frequency. For the initial and final states, the contribution of the moving atom vibrating along the CV DOF, i.e., the so-called attempt frequency, was excluded. The attempt frequency was estimated in the following way: we obtained the second-order derivative (k) of the PES (see Sec. II B 2) at the initial and final states (which are local minima), and computed the corresponding attempt frequency as $\sqrt{k/m}$, where m is the mass of the moving atom (see Sec. II B 3).

The phonon frequencies ω were obtained with the phonopy code [53,54], where we used the MTP potential to compute the atomic forces. We used 216-atom cubic supercells with the lattice constant of 13.248 Å for these calculations.

Note that, based on the harmonic approximation and classical statistics, the change of G_b with T at a fixed lattice constant is due to entropic effects, i.e., to the $-T\Delta S$ term in Eq. (1); the entropic effects result from the thermal excitation of phonons at a fixed lattice constant. The ΔS refers to the entropy change from the initial (or final) to the transition state of a path at a given temperature, determined by the ratio of the respective phonon frequencies [50,51]. Importantly, the phonon frequency can depend on T due to the anharmonicity of interatomic interactions and to the lattice expansion. Here, we adopt the harmonic approximation and anharmonic interactions are neglected; we used the same lattice constant (4.416 Å) for all our calculations. For these reasons, in our study, the phonon frequencies do not depend on T at a fixed lattice constant, and so does not the ΔS. We note that the chosen lattice constant does influence the value of the phonon frequencies, thus the ΔS and the entropic effects on G_b; anharmonic effects may also play a role, although such role was not considered important for the present study as we found that the harmonic approximation describes well the free-energy barrier change with T obtained from MD simulations (see Sec. III C 2).

III. RESULTS

A. Atomic pathways

After irradiation or implantation, various point defects can be created in a SiC sample, including vacancies and interstitials. During a subsequent thermal annealing ($T > \sim 1000$ K), several processes, such as defects' migration and interconversion, can occur; as a result, the VV can be formed by the aggregation of V_C and V_{Si}, if either or both of them are mobile. Here, we mainly consider those defects and defect processes that are relevant to the VV formation and dynamics, and we do not consider the defect generation processes during, e.g., the irradiation step, where VV may be directly created. Interstitials are not considered due to their low barriers ($< \sim 1.5$ eV) for migration or recombination with close vacancies [19,55,56]; they are easily removed in the sample at low temperatures and/or at the early stage of the annealing process. Defects like antisites or dopants are not considered either, as they are immobile at ∼1000 K [1] and thus not directly involved in the VV formation.

Based on previous studies [19–22,24,49,57] and our chemical intuition, the atomic pathways showed in Figs. 1 and 2 were considered. Those in Fig. 1 are the same as in Ref. [24]. We assumed that the transition-state and the barrier of a path would not depend on the orientation of the initial and final defect and thus ignored the defect orientation due to structural distortions. As mentioned above, the migration of mono-vacancies (MV) is required for the generation of VV. We considered the path for V_C [Fig. 1(a)] and V_{Si} [Fig. 1(b)] migration via second-neighbor hops, and the V_{Si} and CAV interconversion [$V_{Si} \rightarrow$ CAV and CAV $\rightarrow V_{Si}$; Fig. 1(b)] as a competing process to the V_{Si} migration. The relative stability of V_{Si} and CAV depends on the E_F [19,24,49,57]. A similar conversion path from V_C to silicon-antisite vacancy (Si_CV_{Si}) was not considered, since Si_CV_{Si} is not a stable complex [49].

As a result of the MV diffusion, vacancies can aggregate into neighboring V_C-V_{Si} pairs (V-V), from which VV can be formed [20,21,24]. We considered the V-V^2 and V-V^3 pairs; due to limitations imposed by the size of our supercell, V-V pairs of larger separations between V_C and V_{Si} were not considered. We studied the pairing of V-V to form VV (V-V → VV) paths in two different cases: (1) the V_C within the V-V^2 (V-V^3) migrates toward the nearby V_{Si} to form VV, denoted as V-V^2 → VV @ V_C (V-V^3 → VV @ V_C); and (2) the V_{Si} within the V-V^2 (V-V^3) migrates toward the nearby V_C to form VV, denoted as V-V^2 → VV @ V_{Si} (V-V^3 → VV @ V_{Si}). The corresponding backward paths were also investigated describing the dissociation of VV into V-V pairs (VV → V-V). These paths are shown in Fig. 1(c).

Additionally, we investigated the rotation (Rot.) and migration (Mig.) properties of VV, which were only briefly discussed in Ref. [19,21,24] and they remain poorly understood. Knowledge of these pathways is critical to control and manipulate the VV orientation and location in device applications. We considered three paths for VV rotational motions [Fig. 2(a)]. The orientation of VV can be changed via the V_C or V_{Si} migration around another MV (Rot. @ V_C or V_{Si}). In particular, we note a two-step pathway (Rot. @ VCV) where an intermediate meta-stable complex $V_CC_{Si}V_C$ (VCV) is involved.

In Fig. 2(b), we present the paths for the VV migration, which can be classified into two categories. The VV can diffuse via the intermediate V-V pairs, where the VV first dissociate and then reassociate. As mentioned above, we only considered the V-V^2 and V-V^3 pairs; the respective paths are denoted as Mig. @ V-V^2 and Mig. @ V-V^3. Given the similarity between the two, we only show the Mig. @ V-V^3 path. The migration paths via V-V pairs with larger separation are not considered, as we expect their barriers to be notably higher. The VV can also diffuse via a rotation mechanism. We present two such paths (Mig. @ V_C and Mig. @ VCV), constructed by combining rotational paths in Fig. 2(a).

B. Energy barriers

We obtained the energy barriers (E_b) of the processes discussed in Sec. III A via the NEB calculations as a function of the charge state q (see Methods). We summarize the E_b obtained at the DDH level of theory in Table I and below we discuss the relative preference of pathways and the influences of charge state on the E_b and thus the defect dynamics.

We find that the barriers for MV migration are higher than ∼3 eV and V_C^{+2} can hardly diffuse ($E_b = 5.22$ eV). The V_{Si} migration barriers are overall lower than those of V_C; hence, the formation of VV would occur mostly due to V_{Si} diffusion. Overall, the V_{Si} and V_C migration barriers decrease with decreasing q, i.e., from positive to negative values. With decreasing q, the barrier for the conversion of V_{Si} to CAV (V_{Si} → CAV) increases, while that of the backward process (CAV → V_{Si}) decreases. Therefore, V_{Si} is more stable when negatively charged; V_{Si} could transform into CAV if positively charged. Our results are consistent with former reports based on DFT calculations [19,20,34,49,57].

Regarding the pairing of V-V to form VV, where one MV migrates toward the other in its vicinity, we find that the barriers of this process are smaller than that of the migration of isolated MVs. For both V-V^2 and V-V^3, the migration of V_{Si} toward V_C (V-$V^{2/3}$ → VV @ V_{Si}) turns out to be the favored path; the migration of V_C toward V_{Si} (V-$V^{2/3}$ → VV @ V_C) presents a higher barrier. These results are consistent with the finding that the V_C migration barriers are larger than those of V_{Si}. In addition, the barriers of V-$V^{2/3}$ → VV @ V_C weakly depend on q, while those of V-$V^{2/3}$ → VV @ V_{Si} decrease with decreasing q. This trend is likely due to the fact that the electrons mostly localize on the V_{Si} within the V-V defects. When the charge state of the V-V changes, only the occupation of the defect levels localized on V_{Si} is affected; hence the charge state of V_{Si} will change, while that of the neighboring V_C remains unaffected; so do their respective migration barriers. We note that the barriers for the backward processes (VV → V-V) are rather large ($E_b >$ ∼3 eV), indicating that the VV is a stable defect in SiC.

In the case of the VV rotation, we find the Rot. @ V_C path is unlikely to occur with barriers $E_b > 5$ eV. The processes Rot. @ V_{Si} and Rot. @ VCV have similar barriers, with $E_b \sim (3,\ 4)$ eV, and the barrier of Rot. @ V_{Si} (Rot. @ VCV) decreases (increases) with decreasing q. Hence, the process Rot. @ V_{Si} (Rot. @ VCV) is favored if VV is negatively (positively) charged.

For the VV migration, we find that the favored process is Mig. @ VCV, with barriers E_b of ∼4 eV that are weakly dependent on q. All other pathways considered here have instead larger barriers ($E_b \sim 5$ eV), and are thus less likely to occur.

Overall our results show that the defect processes studied here depend significantly on the charge-state q, and such dependence is different for different pathways. In addition, we found that multiple, competing pathways may be available for a given process, with both the energy barrier and the preferred pathway depending on the value of q. Therefore, a detailed exploration of available charge states is required to fully understand the defect dynamics at high temperatures. Identifying all possible pathways for a given process is also critical; however, it is extremely challenging, with the NEB method and MD simulations providing valuable, albeit not definitive, insights.

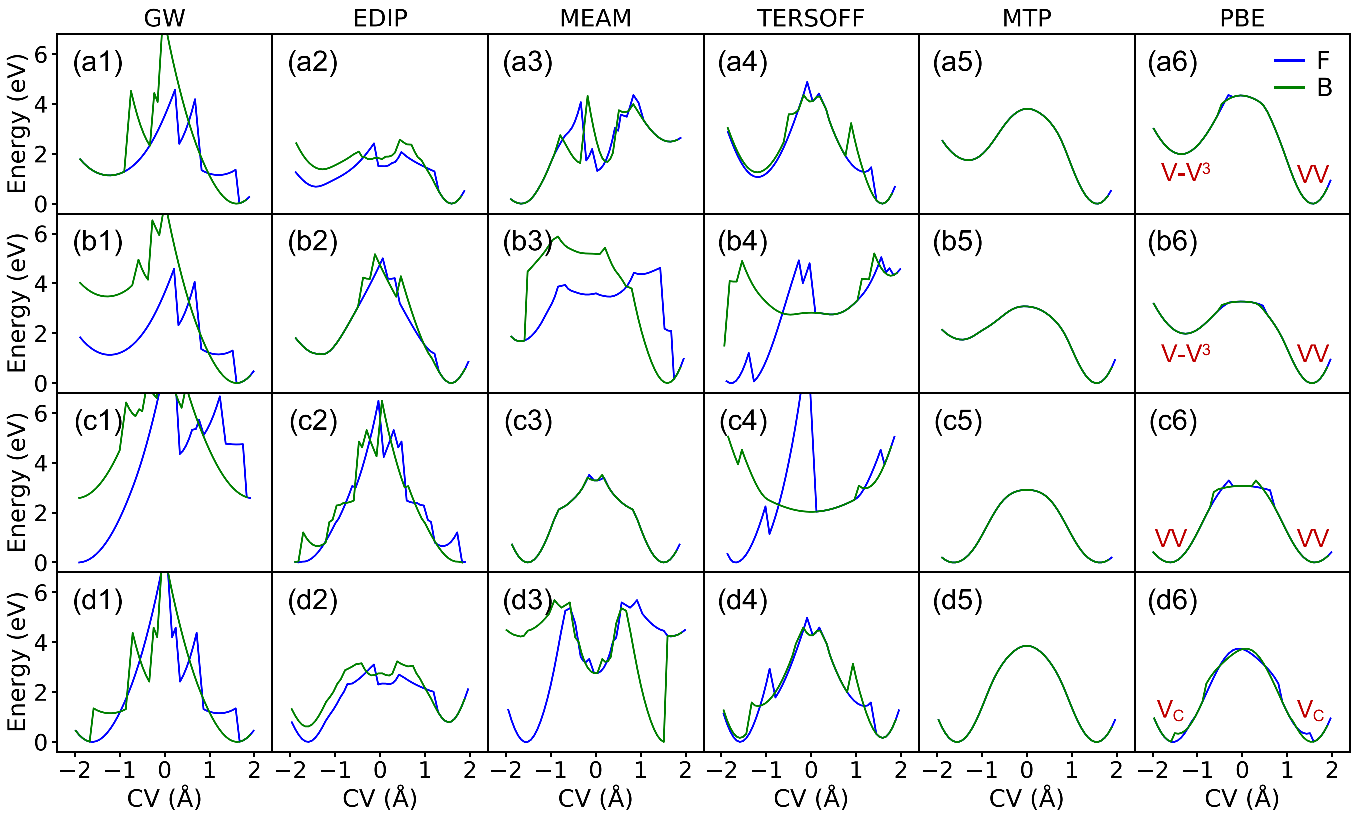

FIG. 3. The computed potential-energy surfaces (PES) at $T = 0$ K as a function of a collective variable (CV). We show results for four pathways (shown in Figs. 1 and 2) in the neutral-charge state: (a) V-V^3 → VV @ V_C (a1)–(a6); (b) V-V^3 → VV @ V_{Si} (b1)–(b6); (c) Rot. @ V_{Si} (c1)–(c6); (d) V_C migration (d1)–(d6). In each column, the results were obtained with the same interatomic potential or DFT functional specified on top of the figure (see Methods). We indicate the initial and final states for each pathway by the red text in column 6 (a6)–(d6); the initial (final) state is on the left (right)-hand side. We show PESs for both the forward (F; shown in blue) and backward (B; shown in green) processes (see Methods).

C. Free-energy barriers and entropic contributions

As shown by Eq. (1), instead of directly computing G_b, we previously approximated G_b using energy barriers (E_b) and the entropic contribution was only estimated. To gain general insights on the entropic effect due to the thermal excitation of phonons on the value of G_b at a fixed lattice constant, here we consider few pathways in 3C-SiC at one single charge state, the neutral-charge state, as examples. An accurate evaluation of G_b and of entropic effects for all relevant pathways and charge states would certainly be desirable; however, it remains challenging, due to the high computational cost of coupling enhanced sampling and FPMD simulations. We first explore the use of classical MD with interatomic potentials, instead of FPMD, to reliably calculate the FES and G_b, and we then examine whether the harmonic approximation is sufficiently accurate to estimate the G_b. These strategies can assist in future studies of defect dynamics at high-T.

1. *Performance of interatomic potentials*

We computed the PESs at $T = 0$ K via constrained optimizations (see Methods) for four pathways, including MV migration, VV formation, and VV rotation processes; we compared results obtained with empirical FFs, the MTP potential, and DFT calculations with the PBE functional, shown in Fig. 3, where the PBE data are considered as reference.

The PESs obtained from empirical FFs are not smooth, most likely because of the short cutoff distance (<∼ 3–4 Å) adopted in the derivation of the force fields. The forward and backward PESs obtained from empirical FFs substantially differ in several cases; sometimes, metastable configurations, that are absent in our calculations using the PBE functional, are explored. In addition, the barriers predicted by empirical FFs are inaccurate, relative to DFT. For instance, the barrier in Fig. 3(a2) is remarkably lower than that in Fig. 3(a6). Also, in Fig. 3(c4), the system is trapped in a metastable configuration after leaving the potential well of VV [at the lower left of Fig. 3(c4)]. Overall the empirical FFs adopted here do not appear to give reliable results, compared to DFT.

Instead, we find a good agreement between the PESs obtained from the MTP model and those of DFT [see also G_b(0-MTP) vs G_b(0-PBE) in Table II]. Unexpectedly, although the isolated V_C migration configurations were not included in the training data, our MTP model can still yield reasonable results [Fig. 3(d5)] for the migration process. This may be due to the fact that the V_C migration may occur via the V-V^3 → VV @ V_C path [Fig. 1(c)], which is included in the training dataset. We observe tiny cusps and hysteresis in PESs obtained from the PBE functional, e.g., in Fig. 3(c6), indicating minor shortcomings of the CV adopted here; nonetheless, the transition state appears to be correctly captured. In Fig. 3(d6), the PESs for the forward and

TABLE II. Free-energy barriers G_b (eV) and the change of free-energy barrier ΔG_b (eV). We show results for four pathways (shown in Figs. 1 and 2) in the neutral-charge state. We show G_b at 0 K and 1500 K obtained using the PBE functional (0-PBE, 1500-PBE) and the MTP potential (0-MTP, 1500-MTP). We obtained G_b at 0 K (1500 K) from PESs at 0 K (FESs at 1500 K) (see Methods). We also show ΔG_b (PBE) = G_b (1500-PBE) − G_b (0-PBE); ΔG_b (MTP) = G_b (1500-MTP) − G_b (0-MTP). Additionally, we estimated the ΔG_b using the harmonic approximation and the MTP potential (MTP-HA). For those paths for which the initial and final states are different (see Fig. 1), we present results for both the forward and backward processes (see Methods); values in parenthesis are for the backward processes.

Pathways	V-V^3 → VV @ V$_C$	V-V^3 → VV @ V$_{Si}$	Rot. @ V$_{Si}$	V$_C$ migration
		G_b		
0-PBE	2.35 (4.34)	1.29 (3.28)	3.07	3.71
1500-PBE	2.24 (4.06)	1.14 (2.98)	2.7	
0-MTP	2.06 (3.81)	1.33 (3.08)	2.91	3.86
1500-MTP	1.89 (3.52)	1.07 (2.7)	2.5	3.51
		ΔG_b		
PBE	–0.11 (–0.29)	–0.15 (–0.29)	–0.37	
MTP	–0.18 (–0.29)	–0.27 (–0.38)	–0.42	–0.35
MTP-HA	–0.2 (–0.27)	–0.31 (–0.37)	–0.42	–0.37

backward processes are not the same but they are symmetrical; this result stems from the two equivalent paths for V$_C$ migration that are symmetrical [49,58]. However, this symmetrical behavior is not exactly captured by the MTP potential [Fig. 3(d5)]. One reason could be the absence of isolated V$_C$ migration configurations in our training data; in addition, our MTP potential was trained using only configurations at 1500 K, and hence may not correctly describe this subtle symmetrical behavior observed at $T = 0$ K.

These comparisons indicate that classical MD simulations using empirical FFs may not be reliable to obtain the FES, G_b as well as entropic effects for defect pathways in SiC, while those using the MTP potential can give more accurate results.

2. *Harmonic approximation for entropic effects*

Using both classical MD and FPMD simulations, we obtained the FESs and G_b at $T = 1500$ K. In classical MD (FPMD) simulations, we used the MTP potential (the PBE functional); we did not use empirical FFs as they appeared to be inaccurate for PESs (see Sec. III C 1).

In Fig. 4, we compare the FESs at $T = 0$ and 1500 K for three pathways, computed using the same lattice constant. We observe that the G_b slightly decreases at high temperature, due to entropic effects [24,50,51]; the trend is the same for the FESs obtained from the MTP potential and the PBE functional. To better understand these observations, we summarize some key quantities in Table II. In addition, we computed the G_b as a function of T using the harmonic approximation (HA; see Methods).

We find the G_b decreases by ∼(0.1, 0.4) eV from 0 to 1500 K (see ΔG_b in Table II). Overall, the MTP potential can reproduce the results of the PBE functional [see ΔG_b(MTP) vs ΔG_b(PBE) in Table II]; we expect that the agreement may be further improved as the accuracy of the MTP potential can be systematically increased. Importantly, the HA can accurately capture the barrier change obtained from enhanced sampling calculations with the MTP potential [see ΔG_b(MTP) vs ΔG_b(MTP-HA) in Table II]. Given that the predictions from the MTP potential and the PBE functional are similar, we expect that the HA can reliably predict the G_b behavior using PBE [ΔG_b(PBE) in Table II]. However, we did not compute ΔG_b using the HA and the PBE functional, since computing phonon frequencies with the DFT method is rather expensive for defective structures with low symmetry.

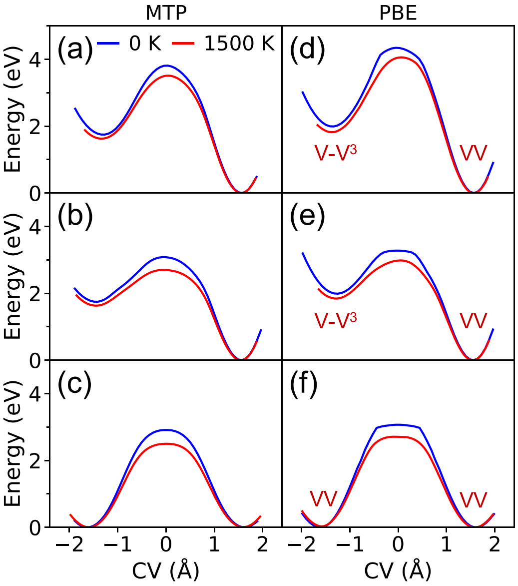

FIG. 4. The computed free-energy surfaces (FES) at $T = 0$ and 1500 K as a function of a collective variable (CV), with the minima of FESs at 0 K and 1500 K aligned. We show results for three pathways (shown in Figs. 1 and 2) in the neutral-charge state: (1) V-V^3 → VV @ V$_C$ (a),(d); (2) V-V^3 → VV @ V$_{Si}$ (b),(e); and (3) Rot. @ V$_{Si}$ (c),(f). The results were obtained using the MTP potential (a)–(c) and DFT simulations with the PBE functional (d)–(f); we specify whether we adopted the MTP potential or the PBE functional on top of each column. We indicate the initial and final states for each pathway by the red text in the second column (d)–(f); the initial (final) state is on the left (right)-hand side. We obtained FESs at 0 K (1500 K) using constrained optimization (enhanced sampling) calculations (see Methods).

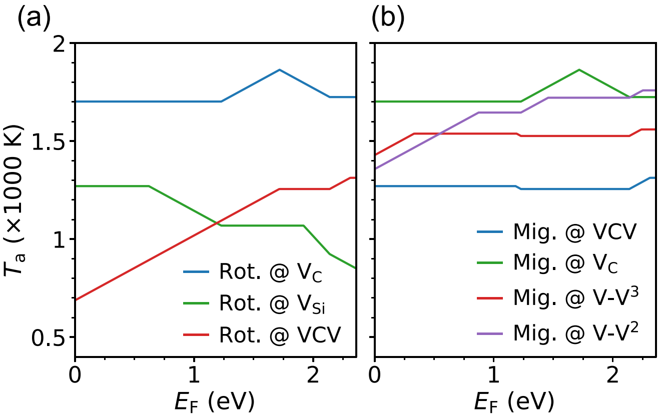

FIG. 5. The activation temperature (T_a) for the divacancy (VV) rotation and migration processes. (a) The T_a for three VV rotation paths as a function of the Fermi level (E_F). (b) The T_a for four VV migration paths as a function of E_F. We refer the E_F to the top of valence band. The atomic pathways are shown in Fig. 2.

Having verified that the HA is valid and accurate to describe the defect processes in SiC, we ascribe the change of G_b with T at a fixed lattice constant to entropic effects from the thermal excitation of phonons, i.e., to the term $\Delta G_b = -T\Delta S$ [see Eq. (1) and discussion in Sec. II B 4]. Overall we find that entropic effects reduce the G_b at finite temperatures, but the reduction is not significant in 3C-SiC; even at 1500 K, the magnitude of ΔG_b is usually $< \sim 10\%$ of G_b. Therefore, we can safely determine the relative preference of various pathways by using energy barriers E_b (i.e., G_b at $T = 0$ K); however, free-energy barriers G_b (including entropic effects) are required to quantitatively predict the defect dynamics. We find that ΔG_b and ΔS are different for different paths, and we also expect them to depend on the charge state. Hence, it would be desirable to use the path- and charge-state-dependent ΔS when approximating G_b at finite temperatures in future studies of defect dynamics.

D. Activation temperature for VV dynamics

Using the energy barriers E_b at various charge states and considering entropic effects due to the thermal excitation of phonons at a fixed lattice constant, we can compute the activation temperature (T_a) above which a given process is thermally activated (see Methods). We note that T_a is useful to design the appropriate annealing temperature in experiments.

In Ref. [24], the processes related to the VV formation were thoroughly studied. Therefore, here, we only discuss the VV rotation and migration processes (see Fig. 2), which are essential to understand the dynamical properties of VV. We do not consider the VV dissociation into isolated MVs, which may occur at very high temperatures. Our results for the activation temperatures are presented in Fig. 5. We find that VV rotational motions can occur at $T < \sim 1000$ K [Fig. 5(a)]. The reorientation mechanism depends on the E_F. Under p-type conditions, the Rot. @ VCV path is favored, while under n-type conditions, the Rot. @ V$_{Si}$ path is favored; under near intrinsic conditions, the two paths are activated at similar temperatures. The Rot. @ V$_C$ path can take place at $T > \sim 1700$ K. We find that the VV starts to diffuse at $T \sim 1300$ K [Fig. 5(b)]. The Mig. @ VCV path is preferred at all E_F values, and its T_a is nearly independent of the E_F, while the other migration processes can occur at $T > \sim 1500$ K. It is worth mentioning that our predicted T_a for VV migration ($\sim$1300 K) is consistent with experimental observations that employing annealing temperatures $>$1300 K leads to a reduction of the VV concentration due to its diffusion (see discussions in Ref. [24]). Further experiments to validate our predictions for the VV reorientation are desired.

Given that E_F depends on T, only a certain range of E_F values in the band gap is accessible under annealing conditions. Here, we consider 1200 K as an example, that is the estimated optimal annealing temperature for the VV formation [24]; we also consider a n or p doping $<10^{18}$ cm^{-3}. According to Supplementary Information Fig. 4 in Ref. [24], the E_F in 3C-SiC should be in the range of $\sim$(0.52, 1.86) eV, relative to the top of the valence band. These values indicate that VV$^{+1/0}$ could be relevant defects, while VV^{-1} is unlikely to be present in the VV dynamics at high T (see Supplementary Information Fig. 1 in Ref. [24]). The case where the VV rotates with low effective barriers [i.e., $T_a \sim (700, 900)$ K] would require the E_F to be close to the band edge [Fig. 5(a)] and hence it is unlikely to occur. For the VV migration, the T_a of the most favorable path (Mig. @ VCV) remains nearly unaffected [Fig. 5(b)] by the narrowing of the available E_F range. These results show that we should consider the Fermi level corresponding to the annealing temperatures of interest to predict the defect dynamics during the annealing experiments.

IV. CONCLUSIONS

By coupling first-principles nudged elastic band calculations and molecular dynamics simulations with enhanced sampling, we investigated the creation, rotation, and migration of the double vacancy VV in 3C-SiC. We found that the VV rotation can be activated below $\sim$1000 K and the VV migration can be activated at $\sim$1300 K. These results complement those on the VV formation reported in Ref. [24], overall providing detailed predictions to control the VV orientation and location in a sample undergoing annealing after irradiation. The energy barriers were computed for various pathways at several charge states and we found that the energy barrier of a given path depends on the charge state and such dependence is different for different paths. Our results showed that several competing pathways may exist for a given process, and their relative preference depends again on the charge state of the defects involved in the process. Entropic effects from the thermal excitation of phonons on the free-energy barriers at a fixed lattice constant were evaluated for few, exemplary pathways in the neutral-charge state, and found to moderately reduce the free-energy barriers by $\sim$(0.1, 0.4) eV from 0 to 1500 K, with the results being again path dependent. We also found that the harmonic approximation is accurate to capture entropic effects and hence evaluate free-energy barriers. Finally, we demonstrated that machine learning potentials, e.g., the MTP model, can correctly describe defect transformation processes in 3C-SiC, while all empirical FFs tested here gave unsatisfactory results. Therefore, classical MD based on machine learning potentials can be a cheaper alternative to FPMD to obtain free-energy surfaces, provided reliable training sets can be generated to obtain the potential. We emphasize that enhanced sampling calculations are critical to obtain proper training configurations near the transition state of a given path and hence reliable machine learning potentials. However, it remains difficult to investigate defect transformations in multiple charge states using interatomic potentials, where one cannot tune the number of electrons of the system, with the treatment of the spin state of defects bringing an additional complexity. While MTP like potentials are useful tools to study paths of a known charge state and generate trajectories of length unaffordable with FPMD simulations, the latter remain the reference method to study the dynamics of spin defects.

Our study indicates that considering all the available charge states of the defects is key to understand and further engineer the point defect dynamics and formation. The charge-state dependence of defect transformation barriers can guide the design of, e.g., the suitable doping condition of the sample and the control of the Fermi level during the high-T annealing, so as to promote or inhibit certain pathways. In addition, the exploration of thermodynamically unstable charge states can lead to lower effective barriers and thus to a more accurate design of annealing temperatures in experiments. To correctly predict the atomistic mechanism of defect dynamics, the ability to access and examine all relevant competing pathways of defect processes is desired; however, such determination remains a nontrivial task. Finally, we expect entropic effects to be significant in determining the free-energy barriers at temperatures higher than considered here, and possibly also in the study of other hosts.

ACKNOWLEDGMENTS

We thank Yu Jin, Elizabeth M.Y. Lee, and Marco Govoni for useful discussions. This work was supported by MICCoM, as part of the Computational Materials Sciences Program funded by the U.S. Department of Energy, Office of Science, Basic Energy Sciences, Materials Sciences, and Engineering Division through Argonne National Laboratory. We acknowledge the computational resources at the University of Chicago Research Computing Center and the Argonne Leadership Computing Facility, which is a U.S. Department of Energy Office of Science user facility at Argonne National Laboratory supported under Contract No. DE-AC02-06CH11357.

---

[1] T. Kimoto and J. A. Cooper, *Fundamentals of Silicon Carbide Technology: Growth, Characterization, Devices and Applications* (John Wiley & Sons, Hoboken, NJ, 2014).

[2] T. Kimoto, Material science and device physics in SiC technology for high-voltage power devices, Jpn. J. Appl. Phys. **54**, 040103 (2015).

[3] B. J. Baliga, Silicon carbide power devices, in *Springer Handbook of Semiconductor Devices* (Springer, New York, 2022), pp. 491–523.

[4] M. Li, X. Zhou, H. Yang, S. Du, and Q. Huang, The critical issues of SiC materials for future nuclear systems, Scr. Mater. **143**, 149 (2018).

[5] T. Koyanagi, Y. Katoh, and T. Nozawa, Design and strategy for next-generation silicon carbide composites for nuclear energy, J. Nucl. Mater. **540**, 152375 (2020).

[6] A. Lohrmann, B. Johnson, J. McCallum, and S. Castelletto, A review on single photon sources in silicon carbide, Rep. Prog. Phys. **80**, 034502 (2017).

[7] S. Castelletto and A. Boretti, Silicon carbide color centers for quantum applications, J. Phys.: Photonics **2**, 022001 (2020).

[8] S. Kanai, F. J. Heremans, H. Seo, G. Wolfowicz, C. P. Anderson, S. E. Sullivan, M. Onizhuk, G. Galli, D. D. Awschalom, and H. Ohno, Generalized scaling of spin qubit coherence in over 12,000 host materials, Proc. Natl. Acad. Sci. USA **119**, e2121808119 (2022).

[9] G. Zhang, Y. Cheng, J.-P. Chou, and A. Gali, Material platforms for defect qubits and single-photon emitters, Appl. Phys. Rev. **7**, 031308 (2020).

[10] W. F. Koehl, B. B. Buckley, F. J. Heremans, G. Calusine, and D. D. Awschalom, Room temperature coherent control of defect spin qubits in silicon carbide, Nature (London) **479**, 84 (2011).

[11] H. Seo, A. L. Falk, P. V. Klimov, K. C. Miao, G. Galli, and D. D. Awschalom, Quantum decoherence dynamics of divacancy spins in silicon carbide, Nat. Commun. **7**, 12935 (2016).

[12] C. P. Anderson, E. O. Glen, C. Zeledon, A. Bourassa, Y. Jin, Y. Zhu, C. Vorwerk, A. L. Crook, H. Abe, J. Ul-Hassan *et al.*, Five-second coherence of a single spin with single-shot readout in silicon carbide, Sci. Adv. **8**, eabm5912 (2022).

[13] D. J. Christle, P. V. Klimov, C. F. de las Casas, K. Szász, V. Ivády, V. Jokubavicius, J. Ul Hassan, M. Syväjärvi, W. F. Koehl, T. Ohshima, N. T. Son, E. Janzen, A. Gali, and D. D. Awschalom, Isolated spin qubits in SiC with a high-fidelity infrared spin-to-photon interface, Phys. Rev. X **7**, 021046 (2017).

[14] G. Wolfowicz, F. J. Heremans, C. P. Anderson, S. Kanai, H. Seo, A. Gali, G. Galli, and D. D. Awschalom, Quantum guidelines for solid-state spin defects, Nat. Rev. Mater. **6**, 906 (2021).

[15] Y.-C. Chen, P. S. Salter, M. Niethammer, M. Widmann, F. Kaiser, R. Nagy, N. Morioka, C. Babin, J. Erlekampf, P. Berwian *et al.*, Laser writing of scalable single color centers in silicon carbide, Nano Lett. **19**, 2377 (2019).

[16] T. Lühmann, J. Meijer, and S. Pezzagna, Charge-assisted engineering of color centers in diamond, Phys. Status Solidi (a) **218**, 2000614 (2021).

[17] D. M. Toyli, C. D. Weis, G. D. Fuchs, T. Schenkel, and D. D. Awschalom, Chip-scale nanofabrication of single spins and spin arrays in diamond, Nano Lett. **10**, 3168 (2010).

[18] A. Csóré, H. J. von Bardeleben, J.-L. Cantin, and A. Gali, Characterization and formation of NV centers in 3C, 4H, and 6H SiC: An *ab initio* study, Phys. Rev. B **96**, 085204 (2017).

[19] X. Yan, P. Li, L. Kang, S.-H. Wei, and B. Huang, First-principles study of electronic and diffusion properties of intrinsic defects in 4H-SiC, J. Appl. Phys. **127**, 085702 (2020).

[20] X. Wang, M. Zhao, H. Bu, H. Zhang, X. He, and A. Wang, Formation and annealing behaviors of qubit centers in 4H-SiC from first principles, J. Appl. Phys. **114**, 194305 (2013).

[21] E. M. Lee, A. Yu, J. J. de Pablo, and G. Galli, Stability and molecular pathways to the formation of spin defects in silicon carbide, Nat. Commun. **12**, 6325 (2021).

[22] U. Gerstmann, E. Rauls, and H. Overhof, Annealing of vacancy-related defects in semi-insulating SiC, Phys. Rev. B **70**, 201204(R) (2004).

[23] M. Bockstedte, A. Gali, A. Mattausch, O. Pankratov, and J. W. Steeds, Identification of intrinsic defects in SiC: towards an understanding of defect aggregates by combining theoretical and experimental approaches, Phys. Status Solidi (b) **245**, 1281 (2008).

[24] C. Zhang, F. Gygi, and G. Galli, Engineering the formation of spin-defects from first principles, Nat. Commun. **14**, 5985 (2023).

[25] J. P. Perdew, K. Burke, and M. Ernzerhof, Generalized gradient approximation made simple, Phys. Rev. Lett. **77**, 3865 (1996).

[26] P. Haas, F. Tran, and P. Blaha, Calculation of the lattice constant of solids with semilocal functionals, Phys. Rev. B **79**, 085104 (2009).

[27] Z. Li and R. Bradt, Thermal expansion of the cubic (3*C*) polytype of SiC, J. Mater. Sci. **21**, 4366 (1986).

[28] G. Henkelman, B. P. Uberuaga, and H. Jónsson, A climbing image nudged elastic band method for finding saddle points and minimum energy paths, J. Chem. Phys. **113**, 9901 (2000).

[29] F. Gygi, Architecture of Qbox: A scalable first-principles molecular dynamics code, IBM J. Res. Dev. **52**, 137 (2008).

[30] S. Kundu, S. Bhattacharjee, S.-C. Lee, and M. Jain, PASTA: Python algorithms for searching transition states, Comput. Phys. Commun. **233**, 261 (2018).

[31] M. Schlipf and F. Gygi, Optimization algorithm for the generation of ONCV pseudopotentials, Comput. Phys. Commun. **196**, 36 (2015).

[32] See Supplemental Material at http://link.aps.org/supplemental/10.1103/PhysRevMaterials.8.046201 for energy barriers of defect processes calculated at the PBE level of theory and collective variables used for atomic pathways.

[33] J. H. Skone, M. Govoni, and G. Galli, Self-consistent hybrid functional for condensed systems, Phys. Rev. B **89**, 195112 (2014).

[34] M. E. Bathen, J. Coutinho, H. M. Ayedh, J. Ul Hassan, I. Farkas, S. Öberg, Y. K. Frodason, B. G. Svensson, and L. Vines, Anisotropic and plane-selective migration of the carbon vacancy in SiC: Theory and experiment, Phys. Rev. B **100**, 014103 (2019).

[35] Y. Liu, P. Stradins, and S.-H. Wei, Air passivation of chalcogen vacancies in two-dimensional semiconductors, Angew. Chem. **128**, 977 (2016).

[36] P. Deák, A. Gali, B. Aradi, and T. Frauenheim, Accurate gap levels and their role in the reliability of other calculated defect properties, Phys. Status Solidi (b) **248**, 790 (2011).

[37] J. F. Binder and A. Pasquarello, Minimum energy path and atomistic mechanism of the elementary step in oxygen diffusion in silicon: A density-functional study, Phys. Rev. B **89**, 245306 (2014).

[38] A. P. Thompson, H. M. Aktulga, R. Berger, D. S. Bolintineanu, W. M. Brown, P. S. Crozier, P. J. in't Veld, A. Kohlmeyer, S. G. Moore, T. D. Nguyen *et al.*, LAMMPS—A flexible simulation tool for particle-based materials modeling at the atomic, meso, and continuum scales, Comput. Phys. Commun. **271**, 108171 (2022).

[39] S. Plimpton, Fast parallel algorithms for short-range molecular dynamics, J. Comput. Phys. **117**, 1 (1995).

[40] F. Gao and W. J. Weber, Empirical potential approach for defect properties in 3*C*-SiC, Nucl. Instrum. Methods Phys. Res. Sect. B **191**, 504 (2002).

[41] G. Lucas, M. Bertolus, and L. Pizzagalli, An environment-dependent interatomic potential for silicon carbide: calculation of bulk properties, high-pressure phases, point and extended defects, and amorphous structures, J. Phys.: Condens. Matter **22**, 035802 (2010).

[42] H. Huang, N. M. Ghoniem, J. K. Wong, and M. Baskes, Molecular dynamics determination of defect energetics in beta-SiC using three representative empirical potentials, Modell. Simul. Mater. Sci. Eng. **3**, 615 (1995).

[43] J. Tersoff, Modeling solid-state chemistry: Interatomic potentials for multicomponent systems, Phys. Rev. B **39**, 5566 (1989).

[44] I. S. Novikov, K. Gubaev, E. V. Podryabinkin, and A. V. Shapeev, The MLIP package: moment tensor potentials with MPI and active learning, Mach. Learn.: Sci. Technol. **2**, 025002 (2021).

[45] A. V. Shapeev, Moment tensor potentials: A class of systematically improvable interatomic potentials, Multiscale Model. Simul. **14**, 1153 (2016).

[46] S. A. Goreinov, I. V. Oseledets, D. V. Savostyanov, E. E. Tyrtyshnikov, and N. L. Zamarashkin, How to find a good submatrix, in *Matrix Methods: Theory, Algorithms and Applications: Dedicated to the Memory of Gene Golub* (World Scientific, Singapore, 2010), pp. 247–256.

[47] E. Darve, D. Rodríguez-Gómez, and A. Pohorille, Adaptive biasing force method for scalar and vector free energy calculations, J. Chem. Phys. **128**, 144120 (2008).

[48] H. Sidky, Y. J. Colón, J. Helfferich, B. J. Sikora, C. Bezik, W. Chu, F. Giberti, A. Z. Guo, X. Jiang, J. Lequieu *et al.*, SSAGES: Software suite for advanced general ensemble simulations, J. Chem. Phys. **148**, 044104 (2018).

[49] M. Bockstedte, A. Mattausch, and O. Pankratov, *Ab initio* study of the migration of intrinsic defects in 3*C*-SiC, Phys. Rev. B **68**, 205201 (2003).

[50] G. H. Vineyard, Frequency factors and isotope effects in solid state rate processes, J. Phys. Chem. Solids **3**, 121 (1957).

[51] J. Li, The mechanics and physics of defect nucleation, MRS Bull. **32**, 151 (2007).

[52] M. E. Tuckerman, *Statistical Mechanics: Theory and Molecular Simulation* (Oxford University Press, Oxford, 2023).

[53] A. Togo, L. Chaput, T. Tadano, and I. Tanaka, Implementation strategies in phonopy and phono3py, J. Phys.: Condens. Matter **35**, 353001 (2023).

[54] A. Togo, First-principles phonon calculations with phonopy and phono3py, J. Phys. Soc. Jpn. **92**, 012001 (2023).

[55] M. Bockstedte, A. Mattausch, and O. Pankratov, *Ab initio* study of the annealing of vacancies and interstitials in cubic SiC: Vacancy-interstitial recombination and aggregation of carbon interstitials, Phys. Rev. B **69**, 235202 (2004).

[56] F. Gao and W. J. Weber, Recovery of close Frenkel pairs produced by low energy recoils in SiC, J. Appl. Phys. **94**, 4348 (2003).

[57] R. K. Defo, X. Zhang, D. Bracher, G. Kim, E. Hu, and E. Kaxiras, Energetics and kinetics of vacancy defects in 4*H*-SiC, Phys. Rev. B **98**, 104103 (2018).

[58] M. Bockstedte and M. Scheffler, Theory of self-diffusion in GaAs, Z. Phys. Chem. **200**, 195 (1997).